Engineering Analysis with Boundary Elements 111 (2020) 195–205

Contents lists available at ScienceDirect

Engineering Analysis with Boundary Elements

journal homepage: www.elsevier.com/locate/enganabound

Assessment of Smoothed Particle Hydrodynamics (SPH) models for predicting wall heat transfer rate at complex boundary

K.C. Ng[a,*], Y.L. Ng[b], T.W.H. Sheu[c], A. Alexiadis[d]

[a] Department of Mechanical, Materials and Manufacturing Engineering, University of Nottingham Malaysia, Jalan Broga, 43500 Semenyih, Selangor Darul Ehsan, Malaysia
[b] Department of Mechanical Engineering, College of Engineering, Universiti Tenaga Nasional (UNITEN), Jalan IKRAM-UNITEN, 43000 Kajang, Selangor Darul Ehsan, Malaysia
[c] Center for Advanced Study on Theoretical Sciences (CASTS), National Taiwan University, Taipei, Taiwan
[d] School of Chemical Engineering, University of Birmingham, Birmingham, United Kingdom

ARTICLE INFO

Keywords:
Smoothed Particle Hydrodynamics (SPH)
Weakly compressible
Dummy particle
Heat transfer
Dirichlet boundary condition

ABSTRACT

Nowadays, the use of Smoothed Particle Hydrodynamics (SPH) approach in thermo-fluid application has been starting to gain popularity. Depending on the SPH boundary condition treatment, different methods can be devised to compute the total wall heat transfer rate. In this paper, for the first time, the accuracies of using the popular dummy particle methods, i.e. (a) the Adami Approach (AA) and (b) the higher-order mirror + Moving Least Square (MMLS) method in predicting the total wall heat transfer rate are comprehensively assessed. The modified equation of the 1D wall heat transfer rate is formulated using Taylor's series. For uniform particle layout, MMLS is first-order accurate. Nevertheless, for an irregular particle layout, its order of accuracy drops to $\sim O(1)$, the order similar to that of the computationally simpler AA. The AA method is then used to simulate several steady and unsteady natural convection problems involving convex and concave wall geometries. The estimated wall heat transfer rate and the flow results agree considerably well with the available experimental data and benchmark numerical solutions. In general, the current work shows that AA can offer a practical means of estimating wall heat transfer rate at reasonable accuracy for problems involving complex geometry.

1. Introduction

Particle methods such as Smoothed Particle Hydrodynamics (SPH), Moving Particle Semi-implicit [15,18,31,32,34,37,49], Dissipative Particle Dynamics [12,36] etc. have been widely used in solving complex fluid dynamics problems nowadays. In particular, SPH is the oldest particle method initially designed to solve astrophysical problems [11,19]. SPH is then extended to solve high-speed compressible flow problems involving shock waves [27]. Unlike the mesh-based method such as the Finite Volume Method [29,30,33,38,39], the convection term is treated exactly in SPH. On the simulation of free-surface flow, it is appealing to note that the implementations of dynamic and shear-free boundary conditions at the free surface are straightforward. The tracking of free-surface location is not necessary at all if the weakly-compressible SPH (WCSPH) model is used. The first attempt of using SPH in simulating free surface problem was reported by Monaghan [26]. Following this pioneering work, a lot of complicated free-surface problems involving splashing, wave breaking and fragmentation of water-air interface have been simulated [7,21,53]. In fact, the application of SPH is not limited to simulating convective-dominated and free-surface problems. Currently, SPH has witnessed its application in solving complex multi-physics problems encountered in bio-medical engineering, food industry, magneto-hydrodynamics, etc. A more complete review on the use of SPH in simulating multi-physics problems has been recently reported [2].

On the modelling of heat transfer using SPH, Cleary is one of the pioneers that has successfully formulated the energy equation in SPH form to model natural convection problem [4]. The method was then extended to solve heat conduction problem in domain with temperature-dependent thermal conductivity [5]. Chaniotis and his co-workers [3] applied the remeshed SPH scheme in solving natural convection problems and good accuracy has been reported. The implicit time integration approach has been used as well to solve the heat conduction problem [41]. In order to account for natural convection problems involving noticeable change of density with respect to temperature, the non-Boussinesq SPH formulation has been proposed [45]. More recently, both Neumann and Robin boundary conditions have been presented in the numerical framework of SPH [9]. The use of SPH in modelling two-phase flow involving phase change has been reported as well [8,50,52].

* Corresponding author.
E-mail addresses: KhaiChing.Ng@nottingham.edu.my, ngkhaiching2000@yahoo.com (K.C. Ng).

https://doi.org/10.1016/j.enganabound.2019.10.017
Received 30 July 2019; Received in revised form 14 October 2019; Accepted 29 October 2019
Available online 11 November 2019

Very recently, the heat transfer process in heat exchanger has been successfully simulated using SPH [14,35].

As compared to the classical mesh-based method, accurate boundary condition modelling using SPH is more complicated due to the truncation of SPH kernel function near the wall. In order to circumvent this issue, the SPH modelling of wall boundary condition follows two basic approaches. In the first approach (*Approach A*), only one layer of wall particles is generated at the wall surface. This procedure could greatly shorten the pre-processing time; however, complex numerical treatment such as the boundary integral method [17,20,23,25] must be performed in order to account for the incomplete near-wall kernel support area by integrating the kernel function onto the boundary intersecting with the kernel support. Unfortunately, it is unclear on how to extend this method to handle arbitrarily complex wall geometry. The above issue can be somehow addressed by applying the Lennard–Jones potential force [28] between fluid and wall particles. Nevertheless, the magnitude of this force must be calibrated for obtaining an accurate SPH solution. The second approach (*Approach B*) involves filling the wall region with particles so that the kernel support region of near-wall fluid particle is fully covered with particles. These particles residing inside the wall region can be either fixed [1,22] or dynamic [6,44]. The dynamic wall particle (or ghost particle) method involves the regeneration of wall particles based on the local wall surface normal and tangent vectors as well as the instantaneous positions of the near-wall fluid particles. Its implementation is complicated when surface geometry involving sharp corners is encountered.

In the current work, we focused on the fixed wall particle (or dummy particle) approach, which is essentially a variant of *Approach B* mentioned above. The dummy particle approach of Adami and his coworkers (denoted as AA in the current paper) has been widely used in isothermal SPH simulation due to the fact that its implementation is simple [1]. That is, the wall surface normal vector is not required while updating the properties of dummy particles. In fact, the AA approach has been previously tested by a series of free-surface flow simulations and the speed and pressure profiles at selected locations agreed quite well with the theoretical and experimental data [47]. Nevertheless, the accuracy of AA in estimating the wall variable such as the total force exerted on a solid body was not assessed. Recently, Guo and his coworkers [13] attempted to fill this gap by applying AA to estimate the total force acting on the floating body. The total force was computed by summing the acceleration terms of all dummy particles inside the floating body. Although the force acting on the floating body was not reported, the time-dependent positions of the floating body were quite agreeable with the experimental data. For flow problem involving heat transfer, the problem of estimating the wall variable such as the total wall heat transfer rate is frequently encountered. For example, while fixing the temperature of wall with baffle plates, the total wall heat transfer rate was then computed to check for any possible heat augmentation [24]. In fact, the method of computing wall heat transfer rate using SPH has been previously put forward in the framework of *Approach A* [5], where boundary density correction is necessary as only one layer of particles is generated at the wall. In the context of ghost particle method, the local wall temperature gradient (or local wall heat transfer rate) can be firstly computed [45], followed by the summation of these local heat transfer rates on the entire wall segment to obtain the total wall heat transfer rate. For the dummy particle approach, since the application of AA in estimating the total wall heat transfer rate has not been reported in open literature, it is unclear to us how this simple method would perform in this regard, particularly when a very complex wall boundary is encountered. Besides that, the accuracy of AA in total wall heat transfer rate prediction as compared to that of using other popular yet complicated higher-order dummy particle method such as the Mirror + Moving Least Square (MMLS) method [22] has not been explored so far.

In this work, we adopted AA in modelling the Dirichlet temperature boundary condition for arbitrarily shaped geometries. By using Taylor's series, we presented first the one-dimensional modified equation of wall heat transfer rate formulated using SPH, followed by comparing the accuracies of AA and other popular higher-order dummy particle method (i.e. MMLS) in predicting the wall heat transfer rate on regular and irregular particle layouts. The necessity of having a more complicated higher-order method in computing the dummy particle temperature on the irregular yet practical particle layout was then assessed. Subsequently, we estimated the wall heat transfer rate in several steady and unsteady natural convection problems involving convex and concave corners. Finally, the numerical results were compared against the available experimental data and benchmark numerical solutions.

2. Mathematical models

The motion of non-isothermal buoyant fluid is governed by the mass balance (continuity) equation:

$$\frac{d\rho}{dt} = -\rho\nabla.\mathbf{v}, \tag{1}$$

the momentum equation:

$$\rho\frac{d\mathbf{v}}{dt} = -\nabla P + \mu\nabla^2\mathbf{v} - \rho\beta\mathbf{g}\left(T - T_r\right), \tag{2}$$

and the energy equation:

$$\rho\frac{dT}{dt} = \frac{k}{C_p}\nabla^2 T. \tag{3}$$

Here, $\mathbf{v}$ and $\mathbf{g}$ are the velocity and gravitational acceleration vectors, respectively, ρ is the fluid density, P is the fluid pressure, T is the fluid temperature, μ is the fluid dynamic viscosity, β is the fluid thermal expansion coefficient, C_p is the fluid specific heat and k is the fluid thermal conductivity. In the current work, the Boussinesq approximation was used to model the buoyancy force. An external upward buoyant force acts on the fluid particle if its temperature is above the reference temperature T_r.

3. Numerical method

3.1. Weakly compressible SPH model

In this work, as the fluid was treated as weakly compressible, the fluid pressure P was expressed as a function of density change:

$$P = c^2\left(\rho - \rho_o\right). \tag{4}$$

Here, c is the speed of sound (10 times the maximum fluid speed in the flow domain) and ρ_o is the initial (reference) fluid density. The discretized versions of Eqs. (1) and (2) using SPH for fluid particle i are:

$$\left\langle\frac{d\rho_i}{dt}\right\rangle = \rho_i\sum\nolimits_j V_j\left(\mathbf{v}_i - \mathbf{v}_j\right)\cdot\nabla_i W_{ij} + 2\delta hc D_i, \tag{5}$$

and

$$\begin{aligned}\left\langle\frac{d\mathbf{v}_i}{dt}\right\rangle = &-\frac{1}{m_i}\sum\nolimits_j\left(V_i^2 + V_j^2\right)\frac{P_i\rho_j + P_j\rho_i}{\rho_i + \rho_j}\nabla_i W_{ij}\\ &+\frac{1}{m_i}\sum\nolimits_j\left(V_i^2 + V_j^2\right)\frac{2\mu_i\mu_j}{\mu_i + \mu_j}\frac{\mathbf{v}_i - \mathbf{v}_j}{\|\mathbf{r}_{ij}\|}\nabla_i W_{ij}\cdot\frac{\mathbf{r}_{ij}}{\|\mathbf{r}_{ij}\|}\\ &-\rho_i\beta\mathbf{g}\left(T_i - T_o\right).\end{aligned} \tag{6}$$

Here, the angled bracket $\langle\blacksquare\rangle$ was introduced to denote an approximated term using SPH. V_j is the volume of neighbouring particle j, i.e. $V_j = m_j/\rho_j$ where m_j is the mass of particle j. According to Sun and his co-workers [43], the parameter δ is a fixed parameter ($\delta = 0.1$). The displacement vector $\mathbf{r}_{ij}$ is defined as $\mathbf{r}_i - \mathbf{r}_j$. The derivative of kernel function $\nabla_i W_{ij}$ is taken with respect to the coordinates of particle i, i.e. $\nabla_i W_{ij} = \frac{dW_{ij}}{dr}\frac{\mathbf{r}_{ij}}{\|\mathbf{r}_{ij}\|}$. In the current work, the quintic spline kernel with

cutoff radius of $r_c = 3h$ was used:

$$W_{ij} = \frac{\alpha_k}{h^D}\begin{cases} (3-s)^5 - 6(2-s)^5 + 15(1-s)^5 & 0 \le s \le 1 \\ (3-s)^5 - 6(2-s)^5 & 1 < s \le 2 \\ (3-s)^5 & 2 < s \le 3 \\ 0 & s > 3 \end{cases} \tag{7}$$

where $s = \|\mathbf{r}_{ij}\|/h$, D is the flow dimension and $\alpha_k = \frac{1}{120}, \frac{7}{478\pi}, \frac{3}{359\pi}$ for $D = 1,\ 2,\ 3$, respectively. In the current work, the smoothing length h was taken as the initial particle spacing d.

In order to suppress the pressure oscillation, the diffusive term D_i was added into the discretized continuity equation:

$$D_i = \sum\nolimits_j (\rho_j - \rho_i) V_j \frac{\mathbf{r}_{ji} \cdot \nabla_i W_{ij}}{\|\mathbf{r}_{ji}\|^2}, \tag{8}$$

3.2. Total wall heat transfer rate

In order to compute wall heat transfer rate, let us consider first the discretized form of Eq. (3) of a local fluid particle i [5]:

$$\left\langle \frac{dT_i}{dt} \right\rangle = \frac{1}{C_p \rho_i} \sum\nolimits_j V_j \frac{4k_i k_j}{k_i + k_j} \frac{\mathbf{r}_{ij} \cdot \nabla_i W_{ij}}{\|\mathbf{r}_{ij}\|^2} (T_i - T_j), \tag{9}$$

Note, the above formulation incorporates the harmonic mean value of thermal conductivity, which is introduced to solve general heat transfer problem involving different materials. Multiplying both sides of Eq. (9) by particle mass m_i and combining the specific heat C_p with $m_i \langle \frac{dT_i}{dt} \rangle$ gives the net rate of change of energy $\langle \frac{dE_i}{dt} \rangle$ [W] of particle i:

$$\left\langle \frac{dE_i}{dt} \right\rangle = \sum\nolimits_j V_i V_j \frac{4k_i k_j}{k_i + k_j} \frac{\mathbf{r}_{ij} \cdot \nabla_i W_{ij}}{\|\mathbf{r}_{ij}\|^2} (T_i - T_j). \tag{10}$$

Here, E_i is the total energy [J] of local fluid particle i.

Note, from Eq. (10), the list of neighbouring particle j of a fluid particle i may consist of both fluid and dummy particles. In order to recover the total heat transfer rate $\langle Q \rangle_w$ to/from the wall from Eq. (10), for all fluid particles i, the contributions of heat transfer rates from all interacting dummy particles are summed:

$$\langle Q_w \rangle = \sum\nolimits_{i \in fluid} \sum\nolimits_{j \in dummy} V_i V_j \frac{4k_i k_j}{k_i + k_j} \frac{\mathbf{r}_{ij} \cdot \nabla_i W_{ij}}{\|\mathbf{r}_{ij}{}^2\|} (T_i - T_j). \tag{11}$$

Following the spirit of dummy particle method, the volume of dummy particle can be fixed as $V_j = d^D$. For the implementation of Dirichlet boundary condition, there are several methods available for estimating the dummy particle temperature T_j in Eq. (11). These methods are discussed in Section 4.1.1.

4. Results and discussions

In this section, firstly, we analysed the order of accuracy of Eq. (11) for 1D heat transfer problem. The most practical dummy particle temperature prediction scheme was then chosen to solve the more complicated natural convection problems including those occurred in complex flow domains with convex and concave corners. For the sake of verification, the computed wall heat transfer rates were then compared with the published numerical/experimental data and those simulated using the established commercial software, i.e. ANSYS FLUENT that employs the Finite Volume Method (FVM). In the current work, the SPH code was parallelized using CUDA C++ and the parallel SPH simulation was executed on a workstation (Intel Xeon 3.7 GHz 16 GB RAM with 1x NVIDIA Quadro P4000 GPU card) at Universiti Tenaga Nasional. On the other hand, the serial FVM simulation was performed using a lab computer (Intel Xeon Bronze 3106 CPU 1.7 GHz 16 GB RAM) at Taylor's University, where the ANSYS FLUENT software license is available.

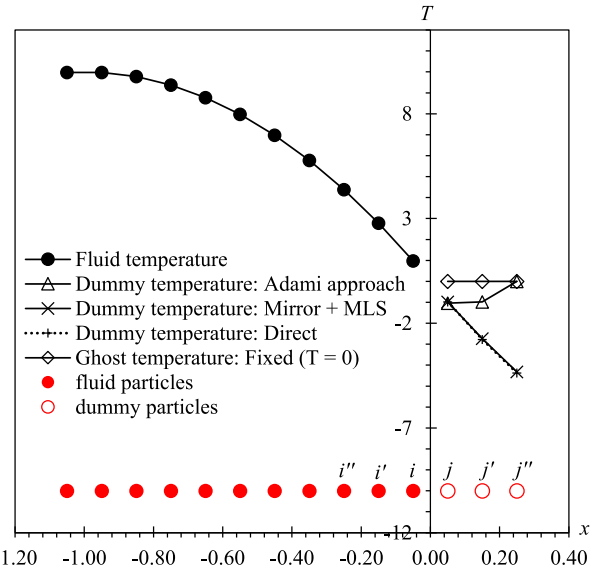

Fig. 1. Estimation of dummy particle temperatures T_j, $T_{j'}$ and $T_{j''}$ (see Eqs. (17) and (18)) using various methods described in Table 1. Wall is located at $x = 0$. Temperatures of fluid particles ($x < 0$) are expressed as $T(x) = -10x^2 - 20x$. The particle spacing is uniform ($d = 0.1$).

4.1. Steady cases

4.1.1. One-dimensional heat conduction problem

For this problem, we intend to compute $\langle Q \rangle_w$ at the wall ($x = 0$) (see Fig. 1) where the analytical solution is available. Here, all the working variables introduced in this sub-section were treated as dimensionless. As shown in Fig. 1, the fluid particles were distributed at $x < 0$ (fluid region) and three layers of dummy particles were generated at $x > 0$ (wall region). In order to test the orders of accuracy of various schemes, the non-linear fluid temperature profile was chosen: $T(x) = -10x^2 - 20x$ where $x < 0$. Therefore, the wall temperature is $T\ (x = 0) = T_w = 0$. By setting the thermal conductivity k to 0.75, the exact solution of the wall heat transfer rate ($Q_w = -kADT/Dx_{x=0}$) is 15. Here, $DT/Dx_{x=0}$ is the temperature gradient at the wall ($x = 0$) and A is the effective heat transfer area. Note, for one-dimensional problem, $A = 1$.

Before we simulate this problem numerically using SPH, let us analyse Eq. (11) using Taylor's series by expanding the fluid particle temperature from that at the wall location (denoted by subscript w). In the current work, we considered only fluid with homogeneous k. As such, Eq. (11) can be rewritten as:

$$\langle Q_w \rangle = \sum\nolimits_{i \in fluid} \sum\nolimits_{j \in dummy} 2k V_i V_j \frac{\mathbf{r}_{ij} \cdot \nabla_i W_{ij}}{\|\mathbf{r}_{ij}{}^2\|} (T_i - T_j) \tag{12}$$

By noting from Fig. 1 that the fluid particles are lying at $x < 0$ and assuming that the fluid temperatures (i.e. T_i, $T_{i'}$, $T_{i''}$) are smoothly varying towards the wall, we can write:

$$T_i = T_w - d_{iw} \frac{DT}{Dx_w} + \frac{d_{iw}^2}{2} \frac{D^2T}{Dx_w^2} + O(d^3) \tag{13}$$

$$T_{i'} = T_w - d_{i'w} \frac{DT}{Dx_w} + \frac{d_{i'w}^2}{2} \frac{D^2T}{Dx_w^2} + O(d^3) \tag{14}$$

$$T_{i''} = T_w - d_{i''w} \frac{DT}{Dx_w} + \frac{d_{i''w}^2}{2} \frac{D^2T}{Dx_w^2} + O(d^3) \tag{15}$$

Here, d_{iw} indicates the distance between particle i and wall position w. By replacing Eqs. (13)–(15) into Eq. (12) and omitting those terms involving two interacting particles with distance apart of above 3 h (Quin-

Table 1
Methods used to estimate $\tilde{T}$ of a generic dummy particle k.

Method	Description
Adami Approach (AA) of [1]	$\tilde{T}_k$ is estimated by simply performing weighted averaging on the neighbouring fluid particles, i.e. $\tilde{T}_k = \frac{\sum_{j\in fluid} T_j W(\|\mathbf{r}_{kj}\|)}{\sum_{j\in fluid} W(\|\mathbf{r}_{kj}\|)}$. This method is computationally simple as the construction of surface normal vector is unnecessary.
Mirror + MLS (MMLS) of [22]	The mirror image of the dummy particle of interest k is generated in the flow domain by using the corresponding surface normal vector. Then, numerical interpolation is performed by using Moving Least Square (MLS) method to compute $\tilde{T}_k$ at every time step. Although this method is more accurate than AA, the generation of mirror images of dummy particles near convex and concave corners is computationally challenging.
Direct	$\tilde{T}_k$ is equivalent to that of its mirror image that coincides exactly with the inner fluid particle. For example, by referring to Fig. 1, $\tilde{T}_j = T_i$, $\tilde{T}_{j'} = T_{i'}$ and $\tilde{T}_{j''} = T_{i''}$. No interpolation is required; however, this method is only applicable for cases employing uniform particle spacing.
Fixed	$\tilde{T}_k$ is equivalent to the wall temperature T_w.

tic spline is used here), the following equation can be obtained:

$$\langle Q_w\rangle = \frac{V_i V_j 2k\left(T_w - d_{iw}\frac{DT}{Dx_w} + \frac{d_{iw}^2}{2}\frac{D^2T}{Dx_w^2} + O(d^3) - T_j\right)}{{d_{ij}}^2} d_{ij}\frac{DW}{Dr_{r=d_{ij}}} + \frac{V_{i'} V_j 2k\left(T_w - d_{i'w}\frac{DT}{Dx_w} + \frac{d_{i'w}^2}{2}\frac{D^2T}{Dx_w^2} + O(d^3) - T_j\right)}{{d_{i'j}}^2} d_{i'j}\frac{DW}{Dr_{r=d_{i'j}}} + \frac{V_i V_{j'} 2k\left(T_w - d_{iw}\frac{DT}{Dx_w} + \frac{d_{iw}^2}{2}\frac{D^2T}{Dx_w^2} + O(d^3) - T_{j'}\right)}{d_{ij'}^2} d_{ij'}\frac{DW}{Dr_{r=d_{ij'}}} \tag{16}$$

Now, the temperatures of dummy particles, i.e. T_j and $T_{j'}$, must be somehow estimated based on the given wall temperature T_w (Dirichlet boundary condition). In the current work, we made use of the following extrapolation procedures:

$$T_j = 2T_w - \tilde{T}_j \tag{17}$$

$$T_{j'} = 2T_w - \tilde{T}_{j'} \tag{18}$$

where $\tilde{T}$ can be predicted using the methods outlined in Table 1. Here, $\tilde{T}$ is the interpolated temperature. For example, $\tilde{T}_{j'}$ is the interpolated temperature at specific location inside the fluid domain which is uniquely associated with the dummy particle j'. Note, for the AA method outlined in Fig. 1, since the dummy particle j'' (furthest away from the wall) does not interact with any fluid particles, $\tilde{T}_{j''} = 0$ (or $T_{j''} = 2T_w - \tilde{T}_{j''} = 2T_w = 0$). By expressing $\tilde{T}$ based on the local wall temperature and its gradient, one can obtain a second-order approximation of $\tilde{T}$:

$$\tilde{T}_j = T_w - d_{jw}\frac{DT}{Dx_w} + O(d^2) \tag{19}$$

$$\tilde{T}_{j'} = T_w - d_{j'w}\frac{DT}{Dx_w} + O(d^2) \tag{20}$$

Substituting Eqs. (17)–(20) into Eq. (16) gives:

$$\langle Q_w\rangle = \frac{V_i V_j 2k\left(T_w - d_{iw}\frac{DT}{Dx_w} - T_w - d_{jw}\frac{DT}{Dx_w} + O(d^2)\right)}{d_{ij}^2} d_{ij}\frac{DW}{Dr_{r=d_{ij}}} + \frac{V_{i'} V_j 2k\left(T_w - d_{i'w}\frac{DT}{Dx_w} - T_w - d_{jw}\frac{DT}{Dx_w} + O(d^2)\right)}{d_{i'j}^2} d_{i'j}\frac{DW}{Dr_{r=d_{i'j}}} + \frac{V_i V_{j'} 2k\left(T_w - d_{iw}\frac{DT}{Dx_w} - T_w - d_{j'w}\frac{DT}{Dx_w} + O(d^2)\right)}{d_{ij'}^2} d_{ij'}\frac{DW}{Dr_{r=d_{ij'}}} \tag{21}$$

By grouping similar terms and rearranging them, Eq. (21) can now be rewritten as:

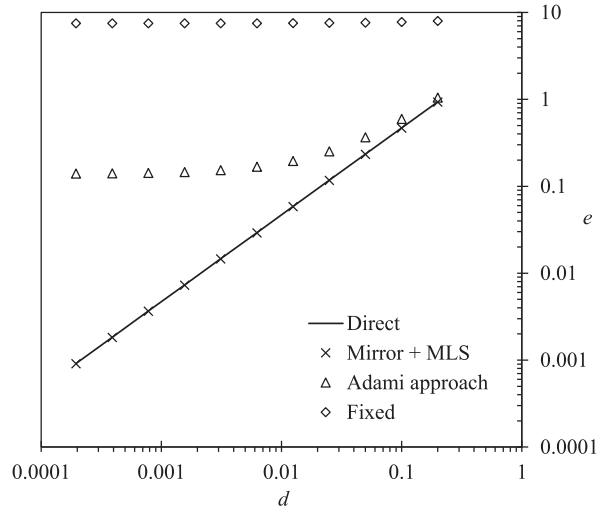

Fig. 2. Spatial convergence tests of various dummy particle temperature extrapolation methods on uniform particle layout. Absolute error e is defined as $e = |\langle Q_w - Q_w\rangle|$.

$$\langle Q_w\rangle = -k\frac{DT}{Dx_w}\left\{2\frac{V_i V_j (d_{iw} + d_{jw})}{d_{ij}}\frac{DW}{Dr_{r=d_{ij}}} + 2\frac{V_{i'} V_j (d_{i'w} + d_{jw})}{d_{i'j}}\frac{DW}{Dr_{r=d_{i'j}}} + 2\frac{V_i V_{j'} (d_{iw} + d_{j'w})}{d_{ij'}}\frac{DW}{Dr_{r=d_{ij'}}}\right\} + O(d) \tag{22}$$

Let us consider the ideal case where the particles are uniformly distributed within the fluid domain (see Fig. 1). One can easily show that the curly bracketed term in Eq. (22) is equal to -1.0 as $V_i = V_j = V_{i'} = V_{j'} = d$, $d_{iw} + d_{jw} = d_{ij}$, $d_{i'w} + d_{jw} = d_{i'j}$, $d_{iw} + d_{j'w} = d_{ij'}$, $\frac{DW}{Dr_{r=d_{ij}}} = \frac{-5}{12d^2}$, and $\frac{DW}{Dr_{r=d_{ij'}}} = \frac{DW}{Dr_{r=d_{i'j}}} = \frac{-5}{120d^2}$. Finally, Eq. (22) becomes:

$$\langle Q_w\rangle = k\frac{DT}{Dx_w} + O(d) = Q_w + O(d) \tag{23}$$

where Q_w is the exact one-dimensional wall heat transfer rate. Considering the negative fluid temperature gradient as outlined in Fig. 1, $\langle Q\rangle_w$ would be negative, thus indicating that the fluid is undergoing heat loss to the adjacent wall modelled by using the dummy particles.

Note, the order of accuracy of Eq. (11) is $O(d)$ if two conditions are met: (1) the particle layout is uniform; and (2) the order of accuracy of $\tilde{T}$ is at least $O(d^2)$ (see Eqs. (19) and (20)). For the case employing uniform particle layout, only MMLS and "Direct" methods (see Table 1) are able to provide the first-order approximation of wall heat transfer rate as witnessed from Fig. 2. The orders of accuracy of AA and "Fixed" approaches, however, are merely $O(1)$. While the absolute error of AA method converges to ~ 0.1, the "Fixed" approach converges to merely half of the exact wall heat transfer rate (i.e. $\langle Q\rangle_w = Q_w/2 = 7.5$,

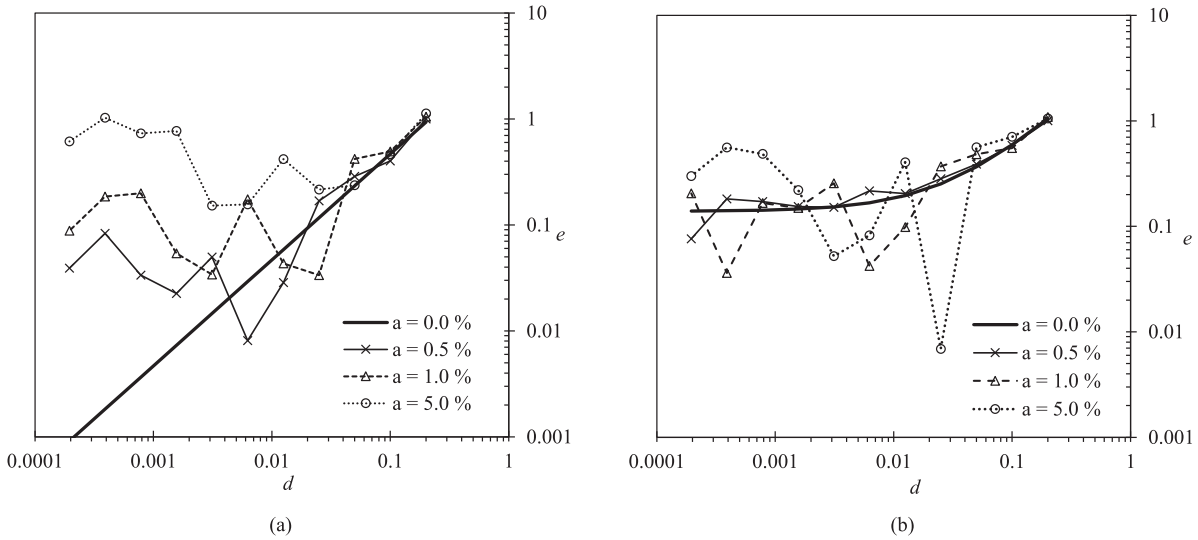

Fig. 3. Spatial convergence tests of (a) MMLS and (b) AA on non-uniform particle layouts for different perturbation amplitudes a. The absolute error e is defined as $e = |\langle Q_w - Q_w \rangle|$.

or $e = |Q_w - \langle Q_w \rangle| = 7.5$). The spatial convergence behaviour of "Fixed" method can be explained by substituting $T_j = T_{j'} = T_w$ into Eq. (16) to obtain $\langle Q \rangle_w = \frac{1}{2} k \frac{DT}{Dx_w} + O(d)$.

In practical SPH simulation, the SPH particles are randomly scattered within the flow field. Plus, in the context of weakly compressible SPH, the volume of fluid particle may be varying as well. In other words, the curly bracketed term in Eq. (22) may not be equal to −1.0, leading to $O(1)$ accuracy of $\langle Q \rangle_w$. In order to simulate the effect of particle non-uniformity, the initial fluid particle positions were perturbed at an amplitude of a% of d. The fluid particle density was then recalculated via: $\rho_i = \sum_j m_j W_{ij}$. While the dummy particle volume was fixed as d, the fluid particle volume V_i was updated as $V_i = m_i/\rho_i$. As shown in Fig. 3(a), the order of accuracy of MMLS approach degrades to $\sim O(1)$ even when the particle positions are perturbed slightly ($a = 0.5\%$). The order of accuracy of AA remains at $\sim O(1)$ on non-uniform particle layout as shown in Fig. 3(b). Owing to the facts that both MMLS and AA methods exhibit the same order of accuracy of $\sim O(1)$ (for $\langle Q \rangle_w$) in the presence of particle non-uniformity and the AA approach is computationally simpler than MMLS, we have decided to employ AA in our subsequent flow simulations.

4.1.2. Natural convection in square cavity

The buoyant flow in a square cavity was simulated and the results were discussed in this section. The length (L) of the square cavity was set to 1.0 m. The temperatures of the left and right walls were fixed at T_H (=T_o + ΔT /2) and T_C (= T_o - ΔT /2), where T_o is the initial fluid temperature (T_o = =300 K) and ΔT is the differential temperature (ΔT = =T_H - T_C). The top and bottom walls, however, were treated as adiabatic. In this case, the working fluid was air with properties: ρ_o = =1.2 kg/m^3, μ = =1.846 × 10^{-5} Pa s, β = =0.0034 K^{-1}, k = 0.0262 W/mK and C_p = =1000 J/kgK. The gravitational acceleration was taken as 9.81 m/s acting in the negative y-direction. Cases of two different Rayleigh numbers (Ra = =$\rho_o{}^2 C_p g \beta \Delta T L^3 / k\mu$), i.e. Ra = =10,000 and Ra = =100,000 were simulated, which correspond to $\Delta T = 1.006984 \times 10^{-4}$ K and ΔT = =1.006984×10^{-3} K, respectively. According to Feng and Ponton [10], the reference speed (U_{ref}) can be calculated via: $U_{ref} = \sqrt{\beta g L \Delta T}$. Hence, the speed of sound c was prescribed as $c = 10 U_{ref}$. As shown in Fig. 4, a rising air stream is visible near the hot (left) wall. The hot air stream exchanges heat with the cold (right) wall, thus loosing certain amount of thermal energy. The cold air drops along the cold wall and regains its thermal energy from the hot (left) wall, forming a closed flow loop within the square cavity. For Ra = =100,000, however, a pair of counter-rotating vortices is visible as shown in Fig. 4(b).

Table 2
Comparison of averaged Nusselt number, Nu_{avg} predicted using different methods. For SPH, the Nu_{avg} is time-averaged from t = 6000 s to t = 10,000 s.

Ra	10,000	100,000
SPH (d = 1/60 m)	2.261	4.580
SPH (d = 1/90 m)	2.249	4.591
FDM [46]	2.243	4.519
FEM [48]	2.254	4.598
DSC [48]	2.155	4.358

The Nusselt number (Nu) distribution ($Nu = -\frac{dT}{dx}\frac{L}{\Delta T}$) along the cold wall was computed and compared with various benchmark solutions. Here, the temperature gradient $\frac{dT}{dx}$ at the cold wall was computed using the Moving Least Square (MLS) procedure [37]. As shown in Fig. 5, the trend of the simulated Nu along the cold wall using SPH is quite similar to those of the Discrete Singular Convolution (DSC) method and the Finite Element Method (FEM) [48]. For both flow cases at different Ra, our predicted Nu values along the cold wall are in general slightly higher than those of DSC. Nevertheless, our SPH results at Ra = =100,000 are very close to the FEM solutions as shown in Fig. 5(b). In order to compare the averaged Nu, i.e. Nu_{avg} at the cold wall, the time evolution of Nu_{avg} was compared with other benchmark solutions and the results were shown in Fig. 6 for different Ra values. Qualitatively, our simulated Nu_{avg} is quite close to those using Finite Difference Method [46] and FEM [48]. Table 2 shows the numerical values of Nu_{avg} predicted using different methods. It is apparent that the DSC solutions for both Ra values are lower than other predictions, including those using the current SPH method. As reported in Table 2, the predicted Nu_{avg} values using SPH at d = 1/60 m and d = 1/90 m agree quantitatively well with those of FDM and FEM.

4.1.3. Natural convection in two concentric cylinders

Next, we intend to investigate the wall heat transfer rate for natural convection occurred between two eccentric cylinders, whereby the experimental data of temperature at various positions are available. This problem has been recently simulated by Yang and Kong [51] using SPH as well. The radii of inner hot (T_H = =323.664 K) and outer cold (T_C = =300 K) cylinders were prescribed as R_1 = =$D_1/2$ = 0.02 m and R_2 = =0.052 m, respectively. The fluid properties were set

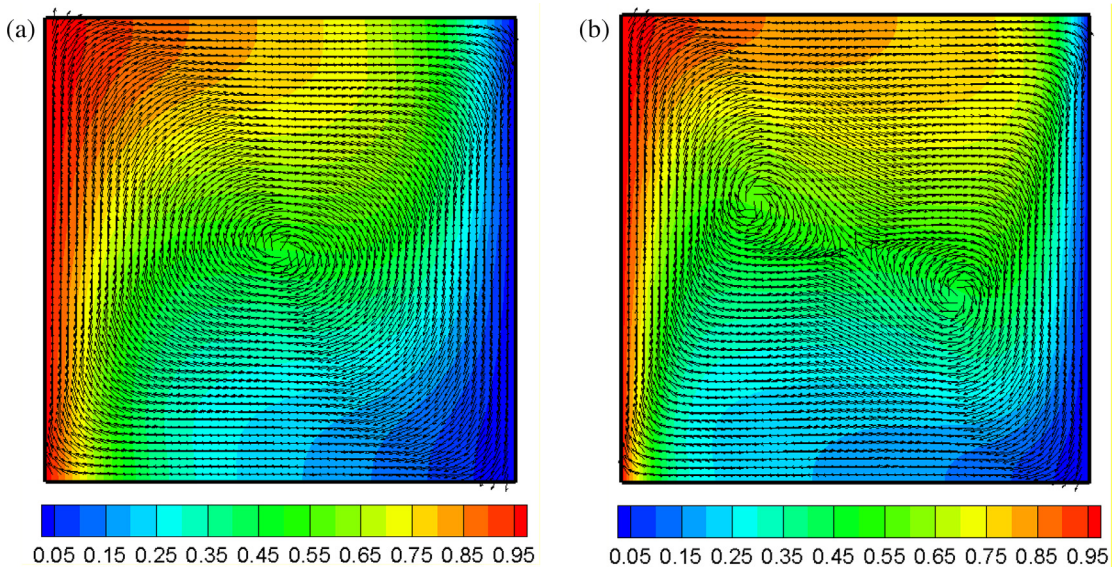

Fig. 4. Predicted velocity vectors and dimensionless temperature contours ($0 < T^* = (T - T_C)/\Delta T < 1$) for (a) Ra = =10,000 and (b) Ra = 100,000 in the square cavity (length $L = 1.0$ m) at $t = 10{,}000$ s. The number of SPH fluid particles is 3600. Note, the SPH results are interpolated to the background Cartesian mesh for contour line generation. The velocity vector length does not correlate with the local speed.

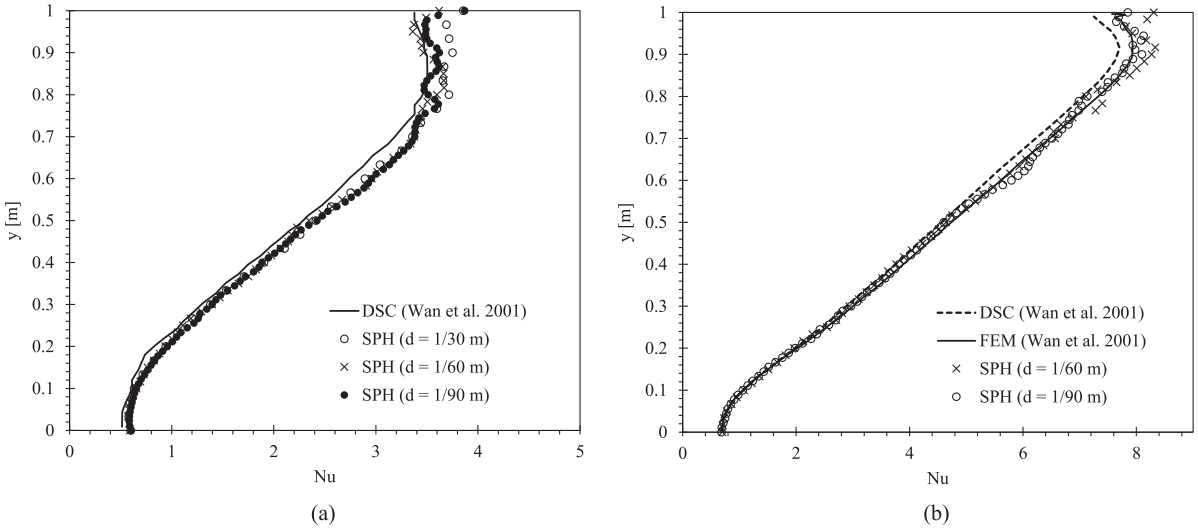

Fig. 5. The variations of Nu along the cold wall for (a) Ra = 10,000 and (b) Ra = =100,000.

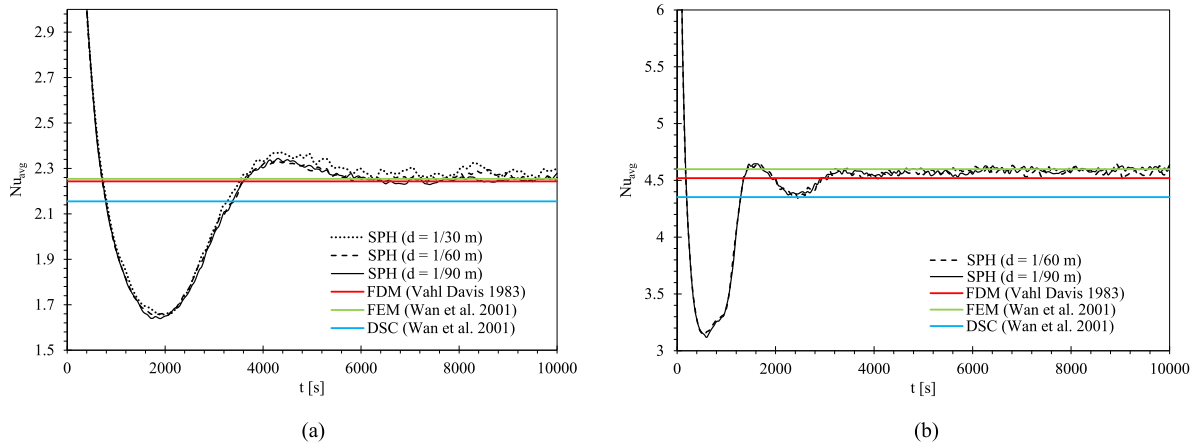

Fig. 6. The time evolutions of averaged Nusselt number, Nu_{avg} for (a) Ra = =10,000 and (b) Ra = =100,000. The sampling size for SPH result is 50 s.

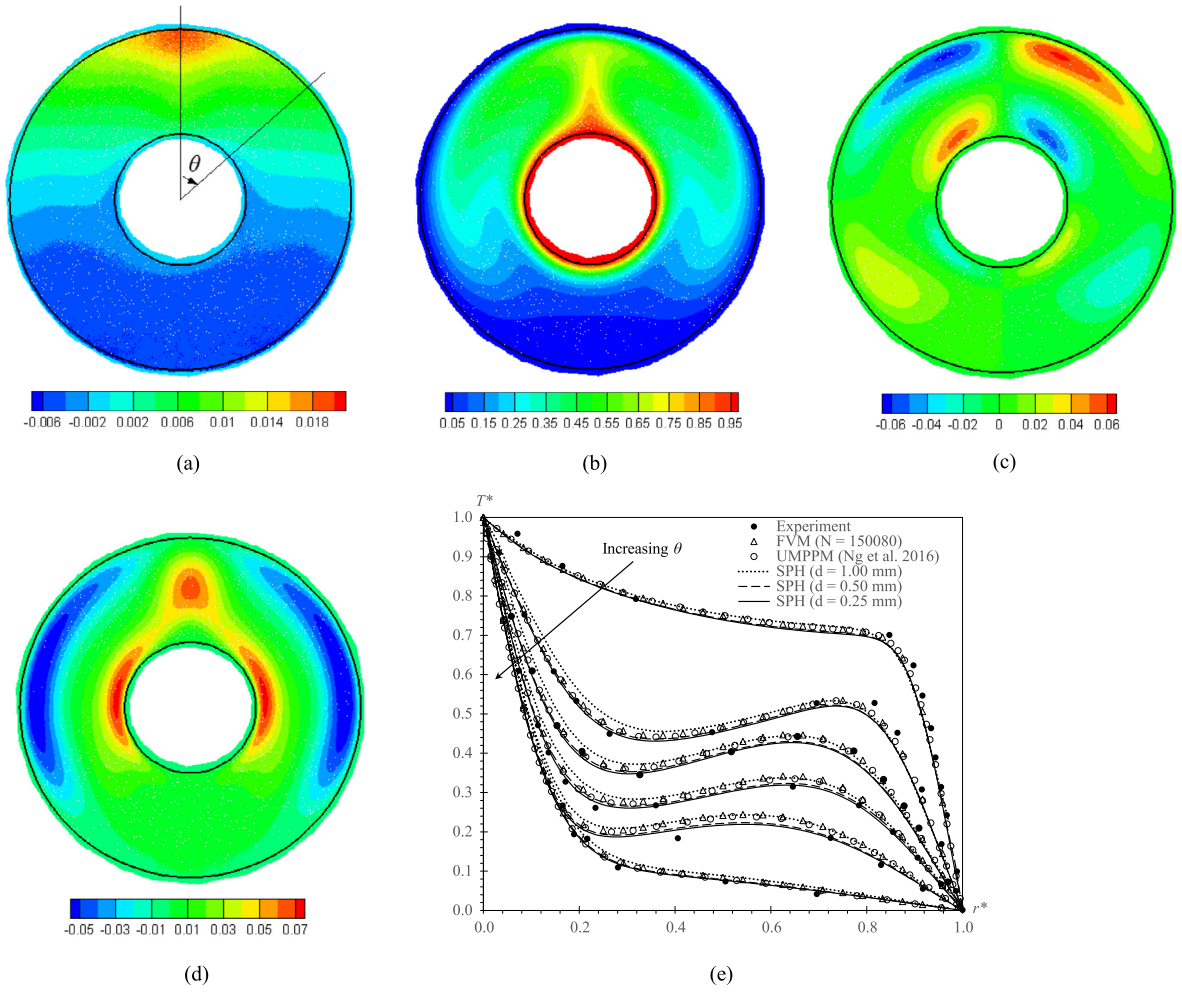

Fig. 7. Steady state results for natural convection in two concentric cylinders. (a) Pressure [Pa]; (b) dimensionless temperature ($T^* = =(T - T_C)/\Delta T$); (c) x-velocity [m/s]; (d) y-velocity [m/s] and (e) distributions of T^* along the dimensionless radial distance ($r^* = =(r - R_1)/(R_2 - R_1)$) at different angular positions (θ), i.e. $\theta = 0$ °, 30 °, 60 °, 90 °, 120 ° and 150 °. N is the total number of meshes used in FVM. SPH results at $t = 20$ s are shown.

to: $\rho_o = =1.096\,\text{kg/m}^3$, $\mu = =2.0\times10^{-5}$ Pa.s, $\beta = =0.003\ K^{-1}$, $k = 0.02816$ W/mK and $C_p = =1006.3$ J/kgK. In this case, the Rayleigh number ($Ra = =\rho_o{}^2 C_p g\beta\Delta T {D_1}^3/k\mu$) is 97,600, where $\Delta T = =T_H - T_C$. The artificial sound speed c was set to 1.69 m/s.

Figs. 7(a)–(d) shows the SPH results obtained at $t = 20$ s using 115,840 fluid particles ($d = 0.25$ mm). The angular position θ shown in Fig. 3(a) is measured from the vertical line passing through the centre of the cylinder. Thanks to the density diffusion term in the continuity equation [22], a smooth pressure field can be attained as shown in Fig. 7(a). The formation of thermal plume above the inner hot cylinder is apparent as shown in Fig. 7(b) and the flow underneath the inner cylinder is mostly isothermal. As shown in Figs. 7(c) and (d), the hot air reaches the top of the flow domain and split into two flow streams. These flow streams travel along the outer curved walls and mix with the hot air streams in the vicinity of the inner cylinder. Following this, two primary flow circulations are formed on both sides of the inner cylinder.

The SPH solutions were then compared against the experimental data [16] and other benchmark numerical solutions obtained using the Finite Volume Method (FVM) and the hybrid Lagrangian–Eulerian UMPPM method [37]. As reported in Fig. 7(e), the grid-independent FVM and UMPPM solutions are almost identical. However, these mesh-based solutions do not coincide with those successively refined SPH solutions. The difference is more discernible at $\theta = =60$ °, 90 °, 120 °. This is expected, as the SPH operators used in the current work are not exactly numerically consistent. The case simulated by using the finest resolution in SPH consists of 115,840 fluid particles ($d = 0.25$ mm), and it is noticed that the results are marginally different from those obtained using the larger particle resolution of $d = 0.50$ mm. Interestingly, for $\theta = =90$ °, 120 ° and 150 °, our SPH solutions employing successively finer particle resolution come closer to the experimental data as compared to those FVM and UMPPM solutions.

Next, we intend to examine the accuracy of AA method in estimating the wall heat transfer rate. Fig. 8(a) shows the time evolution of wall heat transfer rates at both inner and outer cylindrical walls. Both plots plateau at almost the same level at $t > 15$ s, signifying that the steady-state condition is achieved. The steady-state outer wall heat transfer rates were compared against the fine-grid FVM solution ($Q \sim 12.91$ W) as shown in Fig. 8(b). It is noticed that our SPH solutions with $d = 0.50$ mm and 0.25 mm are almost identical ($Q \sim 12.54$ W) at steady-state condition (see Table 3). This wall heat transfer rate value predicted using SPH is somewhat smaller than that using the fine-grid FVM by ~2.8%. This particular issue of numerical inaccuracy might be attributed to the irregular particle layout within the shear-dominated region [40], which is lying adjacent to the circular wall where heat transfer is taking place.

4.2. Unsteady cases

The test cases reported in this section are different from most of the natural convection test cases outlined in open literature that consider

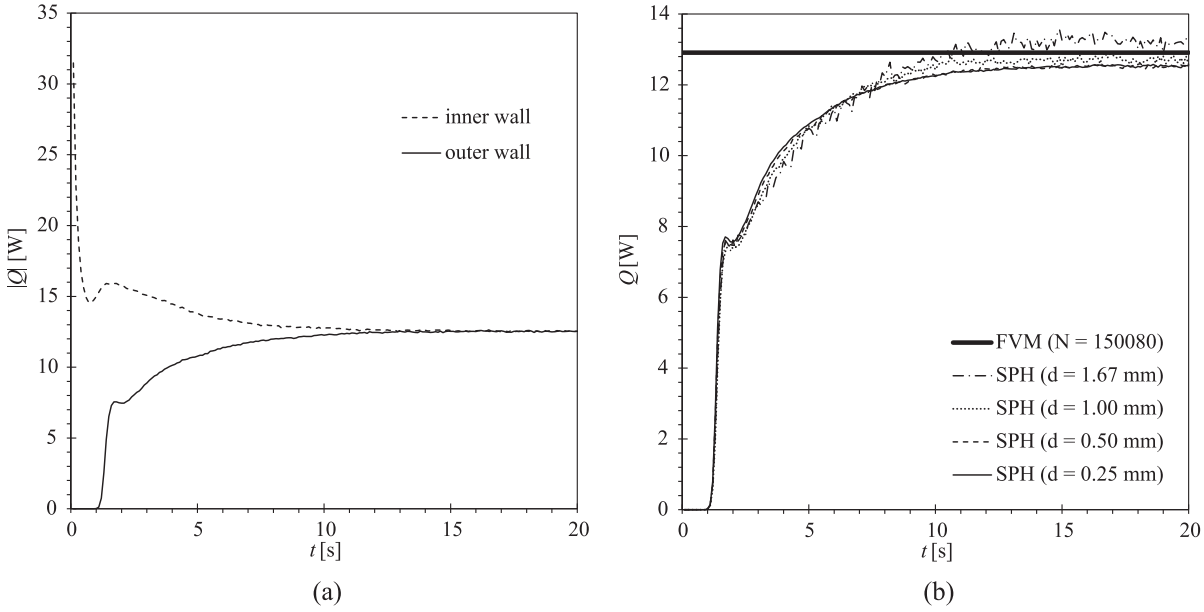

Fig. 8. Time evolution of wall heat transfer rate (Q). (a) $|Q|$ at inner and outer cylindrical walls predicted using Adami Approach (AA) where $d = 0.5$ mm. (b) Effect of particle resolutions on SPH results using AA. The predicted Q using FVM is 12.911 W. N is the total number of meshes used in FVM.

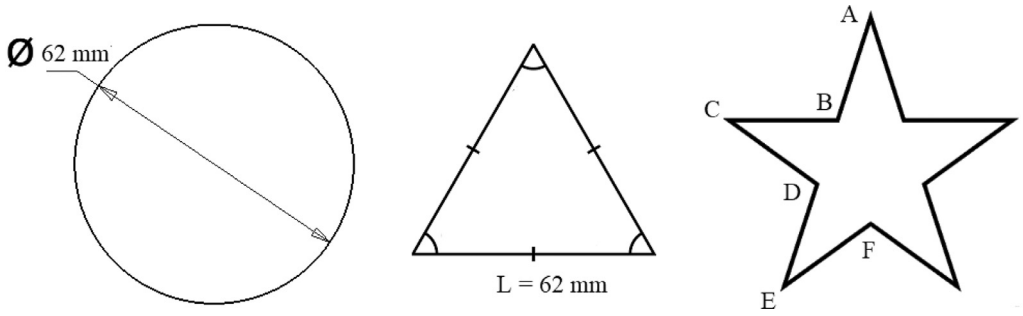

Fig. 9. Unsteady natural convection in circular, equilateral triangular and star cavities. Coordinates of corner points A–F (in mm) in the star cavity are A (31, 62), B (23.746, 38.13), C (0, 38.13), D (19.282, 23.746), E (11.904, 0), F (31, 14.88).

Table 3
Steady-state outer wall heat transfer rate predicted using different numerical schemes. N_{FVM} is the number of meshes (FVM) and N_{SPH} is the number of fluid particles (SPH).

FVM			SPH (at $t = 20$ s)		
d (mm)	N_{FVM}	Q [W]	d (mm)	N_{SPH}	Q [W]
1.670	2166	13.408	1.670	2606	13.376
0.830	8588	13.028	1.000	7223	12.563
0.400	37,760	12.932	0.500	28,968	12.535
0.200	150,080	12.911	0.250	115,840	12.538

buoyancy-driven flow in two differentially heated walls. Here, the hot fluid of initial temperature T_o was encapsulated within an enclosure and the wall temperature was fixed at a lower temperature T_C. Both the buoyancy force acting on the fluid particles and the wall heat transfer rate would decrease as time progresses. Finally, the fluid temperature would be equivalent to the enclosure wall temperature at steady-state condition. In this study, we are interested to study the accuracy of Adami Approach (AA) in predicting the transient wall heat transfer rate.

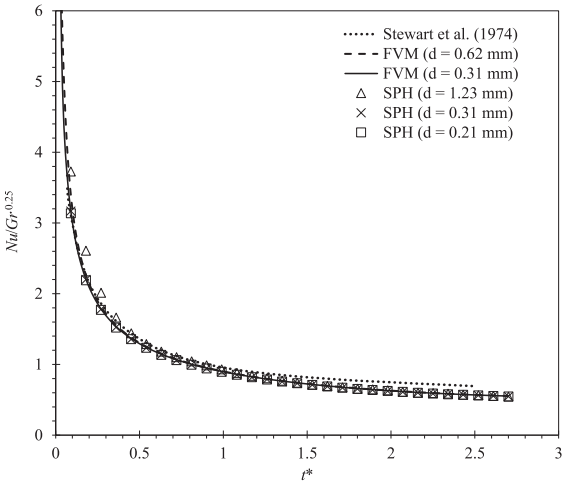

Fig. 10. The decay of wall heat transfer rate at the circular wall.

4.2.1. Circular cavity

One of the few studies that investigates the transient natural convection inside a circular cavity has been reported by Stewart and his co-workers [42]. The circular geometry is shown in Fig. 9, where the diameter is 62 mm ($R = 31$ mm). The following fluid properties were considered in our SPH simulation: ρ_o = =1.2 kg m^{-3}, $\mu = 1.7964 \times 10^{-5}$ Pa s, $\beta = 0.003156\ K^{-1}$, C_p = =1004 J kg^{-1} K^{-1} and $k = 0.02522$ W m^{-1} K^{-1}. Both T_o and T_C were prescribed as 316.826 K

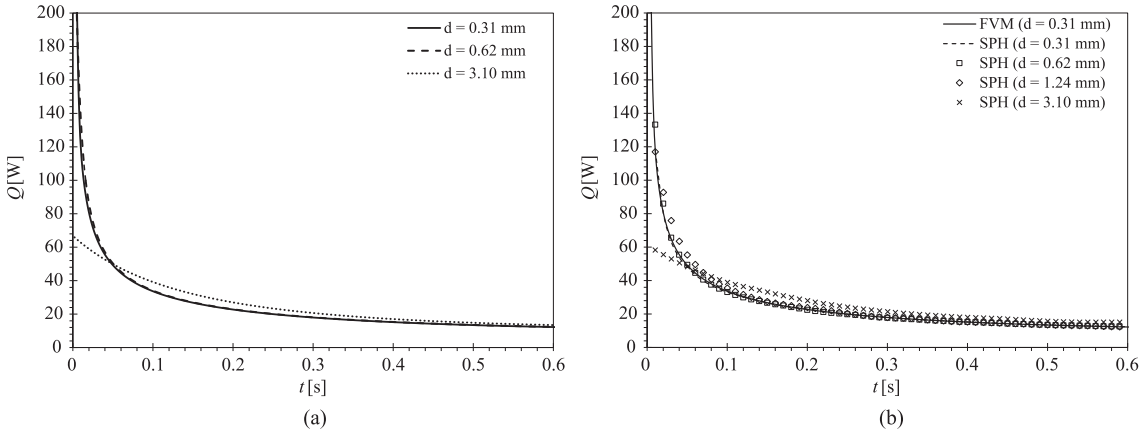

Fig. 11. Time evolution of wall heat transfer rate for triangular cavity. (a) Grid independence test for FVM (ANSYS FLUENT); (b) comparison of FVM and SPH.

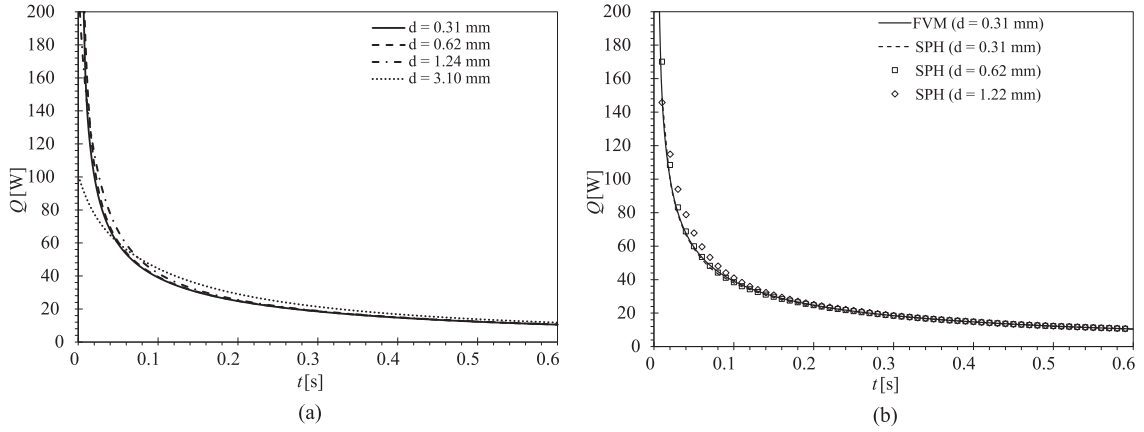

Fig. 12. Time evolution of wall heat transfer rate for star cavity. (a) Grid independence test for FVM (ANSYS FLUENT); (b) comparison of FVM and SPH.

and 296.55 K, respectively. In this case, the Grashof number is defined as $Gr = g\beta(T_o - T_C)R^3/\nu^2 = = 8.35 \times 10^4$, where $g = 9.81$ m s^{-1} and ν is the kinematic viscosity of the fluid. The speed of sound c was set as 2.0 m s^{-1}.

The time evolutions of wall Nusselt number (Nu) predicted using various particle resolutions have been compared with those of Stewart et al. [42] and FVM and the results are shown in Fig. 10. Here, $Nu = 2Rh/k$ where h. is the convection coefficient which can be computed from the wall heat transfer rate: $h = |\langle Q \rangle_w|/[(T_o - T_C)2\pi R]$. The x-axis (dimensionless time) in Fig. 10 can be obtained by normalizing the physical time t [s] with the reference time $t_r = \sqrt{R/[g\beta(T_o - T_C)]}$. As observed from Fig. 10, it is appealing to note that the SPH solutions are almost similar to the grid-independent FVM solution as the particle resolution increases. For FVM, we have used the second-order implicit backward time-stepping scheme by setting the time step size Δt to 0.002 s. In fact, we have found that both wall heat transfer rates predicted using FVM at $\Delta t = 0.001$ s and $\Delta t = 0.002$ s are almost similar. In general, the decaying trend of the wall heat transfer rate is well captured using the SPH method. Meanwhile, the explicit windward-difference solution [42] deviates from the FVM and SPH solutions as time progresses.

4.2.2. Complex cavities

The ability of Adami Approach (AA) in predicting the transient wall heat transfer rate at complex cavity wall has been tested as well. Here, we are particularly interested to observe how AA behaves when this method is applied to compute the heat transfer rate at walls involving sharp corners. As such, a similar transient natural convection study performed earlier has been conducted for a triangular cavity that contains 3 concave corners and a star cavity that contains 5 concave and 5 convex corners. The numerical settings such as fluid properties, initial hot fluid temperature T_o, wall temperature T_C, speed of sound c and gravitational acceleration g are similar to those reported for the case of circular cavity. Both geometries of triangular and star cavities can be found in Fig. 9.

Since the benchmark solution is unavailable, we have performed similar simulation using ANSYS FLUENT and the predicted wall heat transfer rates for triangular and star cavities are shown in Figs. 11(a) and 12(a), respectively. Both FVM results obtained using $d = 0.31$ mm and $d = 0.62$ mm are almost overlapping. We have found similar observation as well for our SPH results shown in Figs. 11(b) and 12(b), in which the SPH solutions are not very sensitive to the particle resolution as $d < 0.62$ mm. As observed, the pattern of decay of $\langle Q \rangle_w$ predicted using SPH at higher particle resolution agrees considerably well with the FVM solution.

The instantaneous speed and temperature fields at $t = 0.6$ s predicted using SPH have been compared to those using FVM and the results are shown in Fig. 13. Good agreement has been found between both sets of result. In both cavities, the inner hot particles experience a slight upward drift from the cavity centre due to the buoyancy force and meanwhile exchange heat with the outer cold wall. The fluid particles are almost stagnant at the corners. The strong descending jets near the side walls of the triangular cavity and the side convex corners of the star cavity are well captured using SPH.

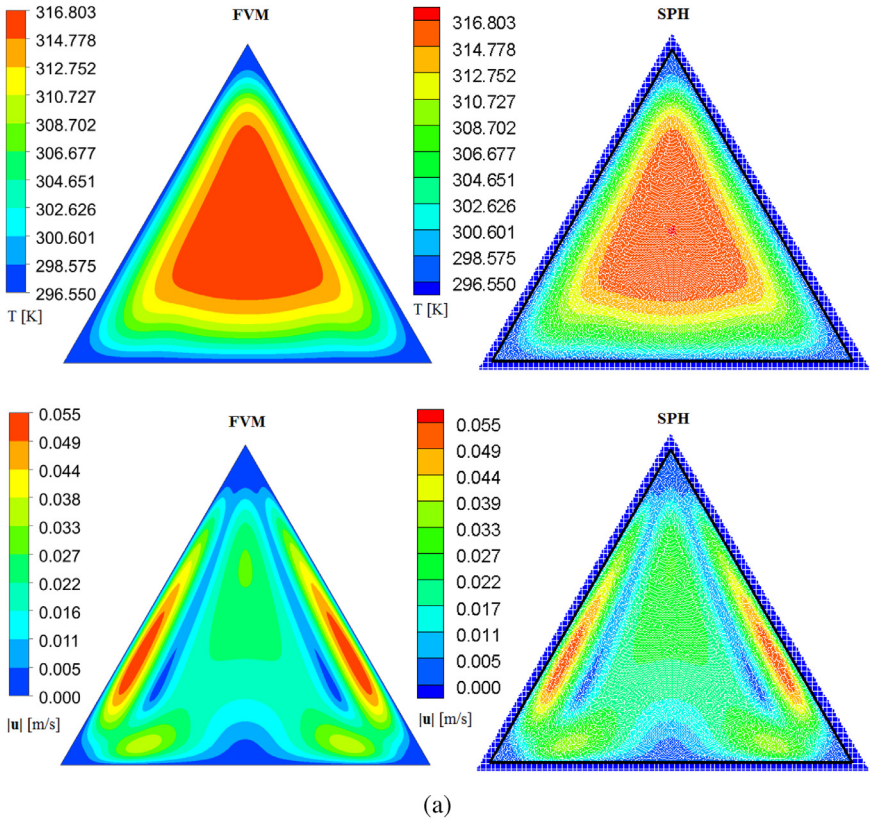

Fig. 13. The instantaneous temperature, T [K] and speed, $|\mathbf{u}|$ [m/s] at $t = 0.6$ s for unsteady natural convections occurred in (a) triangular and (b) star cavities. $d = 0.31$ mm.

5. Conclusion

In this work, the weakly compressible Smoothed Particle Hydrodynamics approach coupled with the dummy particle method has been used to model the Dirichlet temperature boundary condition and to compute the total wall heat transfer rate. The accuracies of the two popular dummy particle methods, namely the Adami Approach (AA) and the Mirror + Moving Least Square (MMLS) method have been comprehensively assessed. Based on the modified equation analysis, the accuracy of the total wall heat transfer rate predicted using the more accurate yet complicated scheme (i.e. MMLS) degrades to $O(1)$ due to the leading error term contributed by particle irregularity. Therefore, the Adami Approach (AA) that exhibits the same order of accuracy of MMLS for an irregular particle layout would be more attractive in practical simulation due to its simplicity in implementation. The AA method has been applied to predict the wall heat transfer rate in complex geometries involving convex and concave corners. The prediction agrees considerably well with the benchmark solutions.

Acknowledgment

The first author would like to thank Taylor's University, Malaysia for allowing him to access the ANSYS FLUENT simulation facility in the computing lab.

References

[1] Adami S, Hu XY, Adams NA. A generalized wall boundary condition for smoothed particle hydrodynamics. J Comput Phys 2012;231:7057–75.
[2] Alexiadis A. The discrete multi-hybrid system for the simulation of solid-liquid flows. PLoS ONE 2015;10(5):1–26.
[3] Chaniotis AK, Poulikakos D, Koumoutsakos P. Remeshed smoothed particle hydrodynamics for the simulation of viscous and heat conducting flows. J Comput Phys 2002;182(1):67–90.
[4] Cleary PW. Modelling confined multi-material heat and mass flows using SPH. Appl Math Model 1998;22(12):981–93.
[5] Cleary PW, Monaghan JJ. Conduction modelling using smoothed particle hydrodynamics. J Comput Phys 1999;148(1):227–64.
[6] Colagrossi A, Landrini M. Numerical simulation of interfacial flows by smoothed particle hydrodynamics. J Comput Phys 2003;191(2):448–75.
[7] Crespo AJC, Altomare C, Domínguez JM, González-Cao J, Gómez-Gesteira M. Towards simulating floating offshore oscillating water column converters with smoothed particle hydrodynamics. Coastal Eng 2017;126:11–26.
[8] Das AK, Das PK. Modeling of liquid-vapor phase change using smoothed particle hydrodynamics. J Comput Phys 2015;303:125–45.
[9] Esmaili Sikarudi MA, Nikseresht AH. Neumann and Robin boundary conditions for heat conduction modeling using smoothed particle hydrodynamics. Comput Phys Commun 2016;198:1–11.
[10] Feng Z, Ponton MC. Smoothed particle method for studying heat and mass transfer between fluid and solid. In: Proceedings of the ASME 2014 International Mechanical Engineering Congress and Exposition IMECE2014; 2014. p. 1–7. November 14–20, 2014.
[11] Gingold RA, Monaghan JJ. Smoothed particle hydrodynamics: theory and application to non-spherical stars. Mon Not R Astron Soc 1977;181(3):375–89.
[12] Groot RD, Warren PB. Dissipative particle dynamics: bridging the gap between atomistic and mesoscopic simulation. J Chem Phys 1997;107(11):4423–35.
[13] Guo K, Sun P-N, Cao XY, Huang X. A 3-D sph model for simulating water flooding of a damaged floating structure. J Hydrodyn 2017;29(5):831–44.
[14] Hosain ML, Domínguez JM, Bel Fdhila R, Kyprianidis K. Smoothed particle hydrodynamics modeling of industrial processes involving heat transfer. Appl Energy 2019;252:113441.
[15] Koshizuka S, Oka Y. Moving-Particle semi-implicit method for fragmentation of incompressible fluid. Nucl Sci Eng 1996;123(3):421–34.
[16] Kuehn TH, Goldstein RJ. An experimental study of natural convection heat transfer in concentric and eccentric horizontal cylindrical annuli. J Heat Transf 1978;100(4):635–40.
[17] De Leffe M, Le Touzé D, Alessandrini B. Normal flux method at the boundary for SPH. In: Proceedings of the fourth SPHERIC workshop; 2009. p. 149–56.
[18] Liu KS, Sheu TWH, Hwang YH, Ng KC. High-order particle method for solving incompressible Navier–Stokes equations within a mixed Lagrangian–Eulerian framework. Comput Methods Appl Mech Eng 2017;325:77–101.
[19] Lucy LB. A numerical approach to the testing of the fission hypothesis. Astron J 1977;82:1013–24.
[20] Macia F, González LM, Cercos-Pita JL, Souto-Iglesias A. A boundary integral SPH formulation consistency and applications to ISPH and WCSPH. Progr Theor Phys 2012;128(3):439–62.
[21] Madhi F, Yeung RW. On survivability of asymmetric wave-energy converters in extreme waves. Renew Energy 2018;119:891–909.
[22] Marrone S, Antuono M, Colagrossi A, Colicchio G, Le Touzé D, Graziani G. δ-SPH model for simulating violent impact flows. Comput Methods Appl Mech Eng 2011;200(13–16):1526–42.
[23] Mayrhofer A, Rogers BD, Violeau D, Ferrand M. Investigation of wall bounded flows using SPH and the unified semi-analytical wall boundary conditions. Comput Phys Commun 2013;184(11):2515–27.
[24] Menni Y, Azzi A, Zidani C. CFD simulation of thermo-aeraulic fields in a channel with multiple baffle plates. J Therm Eng 2018;4(6):2481–95.
[25] Di Monaco A, Manenti S, Gallati M, Sibilla S, Agate G, Guandalini R. SPH modeling of solid boundaries through a semi-analytic approach. Eng Appl Comput Fluid Mech 2011;5(1):1–15.
[26] Monaghan JJ. Simulating free surface flows with SPH. J Comput Phys 1994;110(2):399–406.
[27] Monaghan JJ, Gingold RA. Shock simulation by the particle method SPH. J Comput Phys 1983;52(2):374–89.
[28] Monaghan JJ, Kajtar JB. SPH particle boundary forces for arbitrary boundaries. Comput Phys Commun 2009;180(10):1811–20.
[29] Ng KC. A collocated finite volume embedding method for simulation of flow past stationary and moving body. Comput Fluids 2009;38(2):347–57.
[30] Ng KC, Aziz MAA, Ng EYK. On the effect of turbulent intensity towards the accuracy of the zero-equation turbulence model for indoor airflow application. Build Environ 2011;46(1):82–8.
[31] Ng KC, Hwang YH, Sheu TWH. On the accuracy assessment of Laplacian models in MPS. Comput Phys Commun 2014;185(10):2412–26.
[32] Ng KC, Hwang YH, Sheu TWH, Yu CH. Moving particle level-set (MPLS) method for incompressible multiphase flow computation. Comput Phys Commun 2015;196:317–34.
[33] Ng KC, Ng EYK, Yusoff MZ, Lim TK. Applications of high-resolution schemes based on normalized variable formulation for 3D indoor airflow simulations. Int J Numer Methods Eng 2008;73(7):948–81.
[34] Ng KC, Ng YL, Lam WH. Particle simulation and flow sequence on drainage of liquid particles. Comput Math Appl 2013;66(8):1437–51.
[35] Ng KC, Ng YL, Sheu TWH, Mukhtar A. Fluid–solid conjugate heat transfer modelling using weakly compressible smoothed particle hydrodynamics. Int J Mech Sci 2019;151:772–84.
[36] Ng KC, Sheu TWH. Refined energy-conserving dissipative particle dynamics model with temperature-dependent properties and its application in solidification problem. Phys Rev E 2017;96(4). doi:10.1103/PhysRevE.96.043302.
[37] Ng KC, Sheu TWH, Hwang YH. Unstructured moving particle pressure mesh (UMPPM) method for incompressible isothermal and non-isothermal flow computation. Comput Methods Appl Mech Eng 2016;305:703–38.
[38] Ng KC, Yusoff MZ, Ng EYK. Multigrid solution of Euler equations using high-resolution NVD differencing scheme for unstructured meshes. Progress in Comput Fluid Dyn Int J 2006;6(7):389.
[39] Ng KC, Yusoff MZ, Ng EYK. Higher-order bounded differencing schemes for compressible and incompressible flows. Int J Numer Methods Fluids 2007;53(1):57–80.
[40] Olejnik M, Szewc K, Pozorski J. SPH with dynamical smoothing length adjustment based on the local flow kinematics. J Comput Phys 2017;348:23–44.
[41] Rook R, Yildiz M, Dost S. Modeling transient heat transfer using SPH and implicit time integration. Numer Heat Transf Part B Fundam 2007;51(1):1–23.
[42] Stewart, R.B., Sabol, A.P. and Boney, L.R. (1974), Numerical and experimental studies of the natural convection within a horizontal cylinder, available at: https://ntrs.nasa.gov/archive/nasa/casi.ntrs.nasa.gov/19750004172.pdf.
[43] Sun PN, Colagrossi A, Marrone S, Zhang AM. The δplus-SPH model: simple procedures for a further improvement of the SPH scheme. Comput Methods Appl Mech Eng 2017;315:25–49.
[44] Szewc K, Pozorski J, Minier J-P. Analysis of the incompressibility constraint in the smoothed particle hydrodynamics method. Int J Numer Methods Eng 2012;92(4):343–69.
[45] Szewc K, Pozorski J, Tanire A. Modeling of natural convection with smoothed particle hydrodynamics: non-Boussinesq formulation. Int J Heat Mass Transf 2011;54(23–24):4807–16.
[46] De Vahl Davis G. Natural convection of air in a square cavity: a bench mark numerical solution. Int J Numer Methods Fluids 1983;3(3):249–64.
[47] Valizadeh A, Monaghan JJ. A study of solid wall models for weakly compressible SPH. J Comput Phys 2015;300:5–19.
[48] Wan DC, Patnaik BSV, Wei GW. A new benchmark quality solution for the buoyancy-driven cavity by discrete singular convolution. Numer Heat Transf Part B Fundam 2001;40(3):199–228.
[49] Wang L, Jiang Q, Zhang C. Improvement of moving particle semi-implicit method for simulation of progressive water waves. Int J Numer Methods Fluids 2017. available at:https://doi.org/10.1002/fld.4373.
[50] Yang X, Kong SC. Smoothed particle hydrodynamics method for evaporating multiphase flows. Phys Rev E 2017;96:033309.
[51] Yang X, Kong SC. Numerical study of natural convection in a horizontal concentric annulus using smoothed particle hydrodynamics. Eng Anal Bound Elem 2019;102:11–20.
[52] Yang X, Ray M, Kong SC, Kweon CBM. SPH simulation of fuel drop impact on heated surfaces. Proc Combust Inst 2019;37(3):3279–86.
[53] Zhang DH, Shi YX, Huang C, Si YL, Huang B, Li W. SPH method with applications of oscillating wave surge converter. Ocean Eng 2018;152:273–85.